J. Fluid Mech. (1976), *vol.* 78, *part* 1, *pp.* 99–127
Printed in Great Britain

Time-dependent laminar incompressible flow through a spherical cavity

By N. V. GILLANI AND W. M. SWANSON

Mechanical Engineering Department, Washington University,
St Louis, Missouri 63130

(Received 5 March 1976)

A finite-difference numerical method for the solution of the unsteady flow of a viscous incompressible fluid through axisymmetric circular ducts of variable axial geometry is developed and applied to the flow in a spherical-cavity geometry approximating the human aortic valve. The presence and motion of the valve leaflets are considered only as long as they can be assumed to present negligible impedance to the flow. The numerical solution is based on the vorticity/stream-function approach, and is carried out for the systolic acceleration phase of the heart beat. A hybrid-mesh design consisting of a fine cell structure in the region close to the solid walls and a coarser grid in the core region is used. An experimental flow-visualization study in an acrylic model of the spherical cavity shows good agreement with the numerical simulation. An early separation of flow occurs at the entrance to the cavity, and an annular eddy grows in the wake until it occupies most of the cavity. The use of the hybrid mesh also makes possible the simulation of fine secondary-flow features in the cavity under peak-flow conditions.

1. Introduction

Regions of pronounced axial variation in the cardiovascular flow geometry such as bends, bifurcations, aneurysms and valves are predominant sites of vascular pathogenesis, and haemodynamic factors are believed to play a significant, if not dominant, aetiological role (Texon 1957; Fry 1968; Wessler & Yin 1969; Young & Shih 1969). In particular, pathological conditions in blood vessels are encountered most frequently where flow separation can occur. Various contradictory theories associating low- or high-stress regions with vascular pathologies may be resolved and a better understanding gained of the true nature and manner of haemodynamic influence through a thorough analysis of flow separation in pulsatile flow. Such an analysis can also provide information about the role of the altered flow following separation in governing functional mechanisms such as heart-valve opening and closure (Bellhouse & Talbot 1969). In the present study, a method for the detailed numerical simulation of unsteady separated flows in regions of circular duct variations is developed and applied to simulate the accelerating flow of blood through a spherical-cavity geometry approximating the human aortic valve.

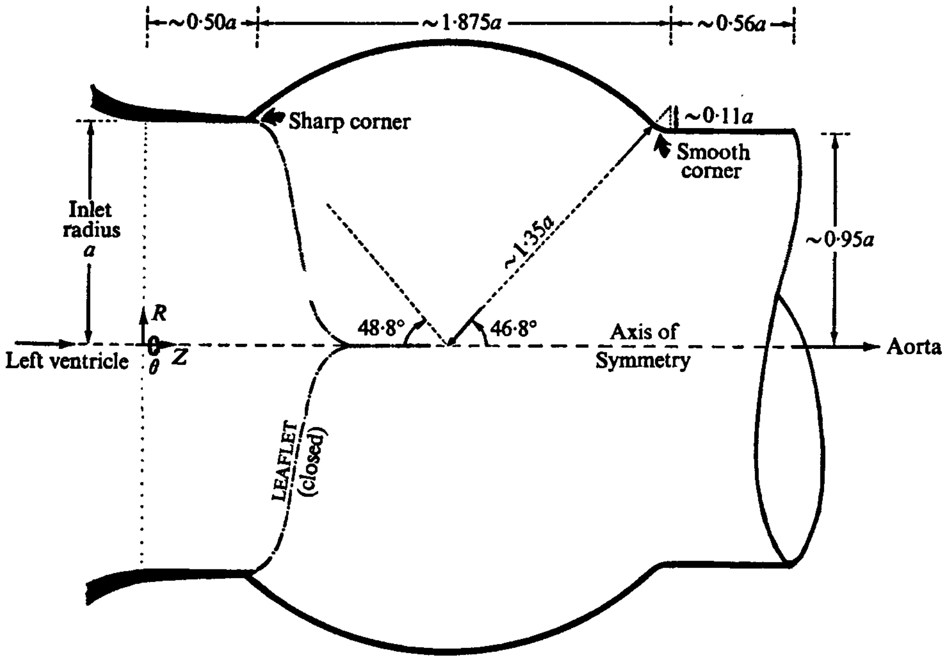

FIGURE 1. Axisymmetric geometry of aortic valve model.

The tricuspid aortic valve is located at the orifice where the aorta emerges from the left ventricle. At the site of the valve, the aortic root bulges to form the sinuses of Valsalva behind the three valve leaflets. The leaflets are thin membranes of neutral buoyancy in blood. Figure 1 shows an idealized axisymmetric geometry of the valve in the closed position. It represents an averaged model based on measurements made in about thirty silicone moulds cast in human aorta for pressures of 0–100 mmHg (Swanson & Clark 1974). In the model geometry, the thick base of the leaflet attachment to the valve ring at the inlet corner of the spherical cavity is approximated by a small but sharp protrusion of the wall into the flow field. The corner at the downstream end is smooth. The aortic diameter downstream of the cavity is slightly smaller than that upstream. The input ventricular flow pulse is shown in figure 2 along with a sinusoidal delivery pulse for comparison. The present work is a numerical analysis of incompressible laminar flow starting from rest and accelerating sinusoidally to peak systole ($t = \frac{1}{2}t_s$) through the modelled axisymmetric, rigid valve geometry.

Laminar flows through rectangular cavities, over steps facing downstream in a channel, and through sudden conduit expansions have been studied both experimentally and numerically, but no systematic study of unsteady flow through spherical cavities in circular ducts has previously been performed. In the numerical simulation of such flows, proper treatment of the boundaries is of crucial importance. A particular contribution of this work is a general treatment of the solid no-slip boundaries. This treatment uses a hybrid system of finite-difference meshing: a coarse cylindrical primary mesh transformed to permit radial compression of the grid away from the centre-line occupies the main flow field and

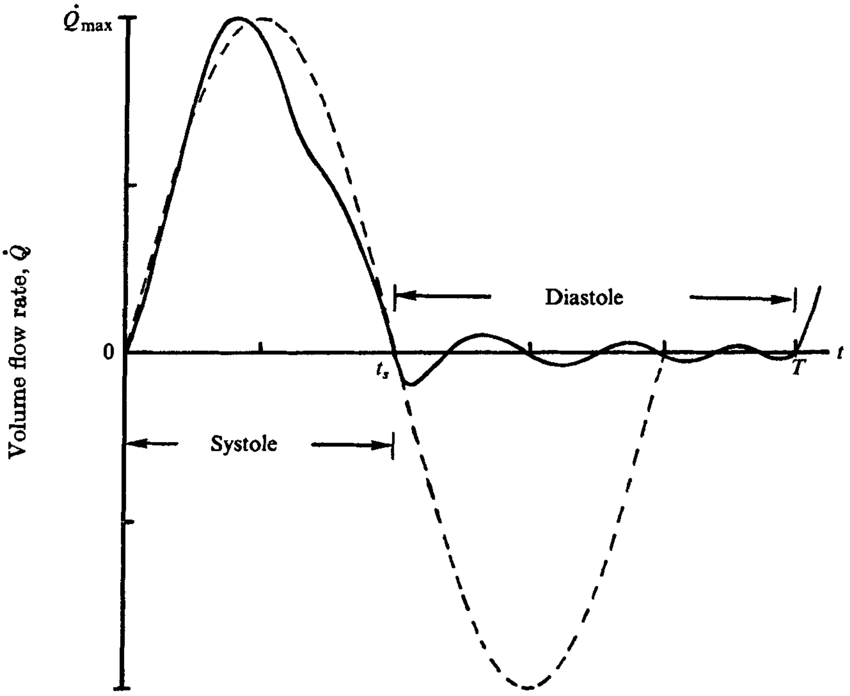

Figure 2. Ventricular flow pulse.

maintains an overall economy of computer usage; in the region close to the wall where the gradients are large, better resolution is obtained by using fine secondary meshes with co-ordinate systems chosen to match the boundary. This method is applicable to duct flows with almost arbitrary axial variations in geometry as long as such variations can be expressed analytically in a piecewise-continuous manner in terms of orthogonal curvilinear co-ordinate systems. The discontinuities may include sharp corners. For example, the method is of direct relevance to the study of unsteady laminar flow within arterial aneurysms, stenoses, and other regions of sudden geometrical vessel variations.

This numerical analysis is first applied to flow in the geometry of figure 1 during the early stages of systolic acceleration, when the leaflets present negligible impedance to the flow. The motion of the leaflets during this early stage of valve opening is traced numerically. During the remainder of the acceleration phase, the computations apply only to the case of the cavity flow with the leaflets not present. An experimental flow-visualization study has been carried out in an acrylic model under conditions approximately similar to those of the numerical model. The numerical solution remains stable throughout the acceleration phase and the corresponding flow closely resembles the observed flow in the physical model. The results provide detailed insight into the development of a captive annular vortex in the spherical cavity. There is also evidence of finer secondary separation and vortices close to the wall, which play a role in controlling the growth and position of the main vortex as peak-flow conditions are approached.

The flow solution at peak systole fits the visual observation of the corresponding flow in the real valve (Bellhouse & Talbot 1969) better than any analytical or numerical solution to date.

2. Previous work

Leonardo da Vinci correctly predicted that vortices would be formed in the sinuses (cavities) of the aortic valve and that they would affect the function of the valve (Keele 1952). Since the systolic acceleration phase lasts for only about $\frac{1}{8}$ s and valve opening takes place within the first 100 ms or so, experimental measurements of the detailed flow characteristics during this short time are not possible. Qualitative flow visualization in physical-model studies by Bellhouse & Talbot (1969) has shown, however, that "vortices are formed early in systole, reached maximum strength at peak systole, and persisted well into diastole" Also, it was observed in the same study that near peak-flow conditions the vortex core was displaced from the cavity centre towards the downstream corner.

The dynamic interaction between the moving boundaries of the valve and the three-dimensional flow field cannot be handled fully at this time even in detailed numerical studies. Peskin (1972) approached the problem by replacing the flexible valve leaflets and an elastic wall constrained to return to equilibrium following any disturbance "by a field of force which is defined on the mesh points of a rectangular domain, and which is calculated from the configuration of the boundary". Computer limitations, however, restricted the maximum Reynolds number at which stable numerical solutions could still be obtained to one or two orders of magnitude lower than those attained in the human aorta. Hung & Schuessler (1971) and Schuessler & Hung (1972) performed a numerical analysis of potential flow within a rigid axisymmetric valve geometry. Leaflet motion was adjusted to produce a desired pressure drop across the valve during opening. A cylindrical mesh system was employed in the entire flow field including the region near the curved walls. No vortex formation was obtained during valve opening.

Laminar incompressible flows over cavities, abrupt steps and bluff bodies with splitter plates in their wakes have the following common features: boundary-layer growth upstream of the impending flow separation, separation of flow and its subsequent reattachment further downstream, a separation wake consisting primarily of a recirculating vortex with possible secondary vortices, and a free shear layer of concentrated vorticity along the separation streamline. The energy to sustain the wake flow is derived from the main flow itself and is transferred across the free shear layer. The size of the wake region generally increases with the free-stream Reynolds number (Macagno & Hung 1967; Mueller & O'Leary 1970).

Batchelor (1956) considered steady laminar flow with closed streamlines at high Reynolds number and showed that viscous forces are concentrated in shear layers outside the main recirculating eddy and produce constant vorticity within the eddy, the magnitude of the vorticity depending on the conditions of the external flow. Burggraf (1966), Pan & Acrivos (1967) and others obtained steady-flow solutions for two-dimensional rectangular cavities at low Reynolds number, and Gosman *et al.* (1969) considered the same flow at Reynolds numbers up to 10^4. Mehta & Lavan (1969) and Donovan (1970) carried out corresponding solutions for the unsteady case. Tani (1968), Roach & Mueller (1970) and, most recently, Honji (1975) studied flow down a rearward-facing step. Honji's experiments demonstrated clearly the existence of secondary vortices which formed when the recirculating flow behind the step itself separated from the base. Macagno & Hung (1967) investigated flow in a sudden axisymmetric conduit expansion numerically and experimentally, and Back & Roschke (1972) performed similar experiments. Bearman (1965) observed the presence of secondary vortices in experimental studies of separated flow behind a bluff body fitted with a splitter plate in the wake. Thoman & Szewczyk (1969) used a hybrid cell structure in the numerical simulation of flow around a cylinder and obtained secondary vortices in the wake. Honji & Taneda (1969) made similar observations experimentally. In a more recent experiment by Scherer (1973), steady flow through axisymmetric glass models of aneurysms (spherical cavities) was studied by flow visualization and surface-pressure measurements. The principal observation was a clear separation of flow for each of three cavity-to-duct radius ratios. The separation occurred at the bulb entrance, and a captive vortex, whose size depended on the inlet Reynolds number, occupied the cavity.

3. Mathematical formulation

Basic equations

Blood may be assumed to be an incompressible Newtonian fluid in the flow range considered. For the laminar axisymmetric flow of such a fluid, the flow equations are conveniently expressed in terms of a transport equation for vorticity ω and a coupled equation for the Stokes stream function ψ. The vorticity-transport equation is

$$\partial\boldsymbol{\omega}/\partial t = \nabla\times(\mathbf{v}\times\boldsymbol{\omega}) + \nu\nabla^2\boldsymbol{\omega}, \tag{1}$$

where $\boldsymbol{\omega} = \nabla\times\mathbf{v} = \omega\hat{\boldsymbol{\theta}}$, θ is the azimuthal co-ordinate and ν is the kinematic viscosity. The stream-function equation has the form

$$L_2(\psi) = r\omega, \tag{2}$$

where L_2 is a linear second-order partial differential operator, the precise form of which depends on the choice of co-ordinate system, for example the forms in (6) and (10) below, and r is the radial distance from the axis of symmetry.

The nonlinear term $\nabla\times(\mathbf{v}\times\boldsymbol{\omega})$ in (1) may also be written as $(\boldsymbol{\omega}.\nabla\mathbf{v}-\mathbf{v}.\nabla\boldsymbol{\omega})$. In the latter form, the first term $(\boldsymbol{\omega}.\nabla\mathbf{v})$ represents the rate of vortex-line stretching, and the second term $(\mathbf{v}.\nabla\boldsymbol{\omega})$ represents the rate of vorticity convection. The stretching of vortex lines is most pronounced in the vicinity of abrupt changes in the flow geometry. When an accelerating flow starts from rest, a continuous generation of vorticity at the solid walls is initiated in direct response to the need to satisfy the no-slip condition. Subsequently, molecular diffusion of this vorticity into the flow field causes boundary-layer growth. Vortex-line stretching and

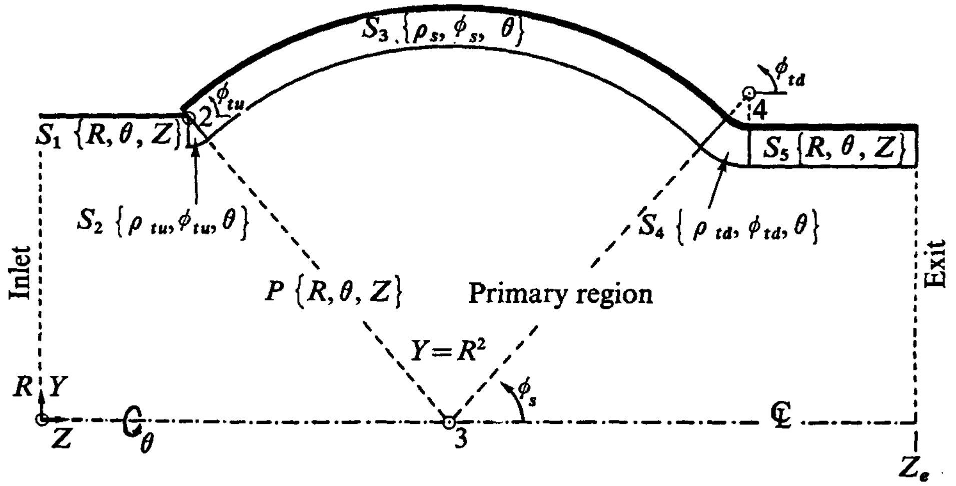

FIGURE 3. Regions of the hybrid-mesh system. P, primary region in which radial co-ordinate transformation $Y = R^2$ is made; S_1, upstream secondary cylindrical region; S_2, upstream secondary toroidal region; S_3, secondary spherical region; S_4, downstream secondary toroidal region; S_5, downstream secondary cylindrical region. (All lengths, e.g. R, Z, ρ, are normalized with respect to inlet radius a.)

convection feature increasingly in the redistribution of vorticity as the flow accelerates, and, at high Reynolds numbers, their effects dominate viscous damping, ultimately leading to physical as well as numerical instabilities.

The accurate determination of the wall vorticity is of considerable importance because vorticity is generally concentrated in the shear layers adjacent to the solid walls. It has been demonstrated that errors introduced in computations of the boundary-layer vorticity do not decay rapidly away from the boundary and often dominate truncation errors (Cheng 1969). In the core region, on the other hand, gradients of the flow variables are generally small. In view of the need both for accuracy and for economy of computational resources, it is therefore most desirable to design the finite-difference mesh such that mesh cells near the solid walls are small and locally aligned with the wall, while those in the core region are relatively coarser and parallel to the axis of symmetry. To attain these features, the region of flow is divided into a primary region and a number of secondary regions, as shown in figure 3. A separate axisymmetric co-ordinate system is selected for each region. The primary region consists of a cylindrical system with the following transformation of the radial co-ordinate R ($= r/a$):

$$Y = R^2. \tag{3}$$

The effect of the transformation is to make equal intervals ΔY in the transformed plane (Y, Z) correspond to non-uniform intervals ΔR (proportional to $1/R$) in the real plane (R, Z). Thus the desired effect of radial compression of the mesh as the walls are approached is achieved while a uniform radial mesh size (ΔY) is retained in the computations. The secondary regions consist of cylindrical systems along the straight inlet and outlet walls, a spherical system along the curved sinus wall, and toroidal systems for both corner regions. The co-ordinates ρ and ϕ of the spherical and toroidal systems are defined with respect to local centres: O_3 for the spherical system, and O_2 and O_4 for the upstream and downstream toroidal systems respectively.

In the non-dimensionalization of the flow equations, the inlet radius a and beat period T are used as the reference length and time. The mean systolic velocity averaged over the inlet cross-section is taken as the reference velocity $\langle\overline{w}\rangle$, and is computed from

$$\langle\overline{w}\rangle = Q_f/\pi a^2 t_s, \tag{4}$$

where Q_f is the total systolic flow volume. The vorticity ω and stream function ψ are normalized using $\langle\overline{w}\rangle/a$ and $a^2\langle\overline{w}\rangle$ respectively, and are then denoted by η and ξ. In the primary system (Y, θ, Z), the normalized vorticity-transport equation is

$$\frac{\partial\eta}{\partial t'} = -\frac{1}{N_{\mathrm{str}}}\left[2Y^{\frac{1}{2}}\frac{\partial(U\eta)}{\partial Y}+\frac{\partial(W\eta)}{\partial Z}\right] + \frac{1}{\tilde{N}_R}\left[4\frac{\partial}{\partial Y}\left(Y\frac{\partial\eta}{\partial Y}\right)-\frac{\eta}{Y}+\frac{\partial^2\eta}{\partial Z^2}\right], \tag{5}$$

and the normalized stream-function equation is

$$4Y\frac{\partial^2\xi}{\partial Y^2}+\frac{\partial^2\xi}{\partial Z^2} = Y^{\frac{1}{2}}\eta. \tag{6}$$

In the above equations, Y and Z are dimensionless co-ordinates, t' is the dimensionless time, and U and W are the dimensionless velocity components in the Y and Z directions respectively. Two independent characteristic system parameters are identified: the Strouhal number $N_{\mathrm{str}} = a/\langle\overline{w}\rangle\, T$ and the pulsatile Reynolds number $\tilde{N}_R = a^2/\nu T$. A Reynolds number for the mean flow may also be defined as

$$N_R = \langle\overline{w}\rangle\, a/\nu = \tilde{N}_R/N_{\mathrm{str}}.$$

By the definition of the stream function, $\xi(Y, Z)$ will satisfy the continuity equation with the velocity components given by

$$U = Y^{-\frac{1}{2}}\,\partial\xi/\partial Z, \quad W = -2\,\partial\xi/\partial Y. \tag{7}$$

The scalar component of vorticity is

$$\eta = \partial U/\partial Z - 2Y^{\frac{1}{2}}\,\partial W/\partial Y. \tag{8}$$

Substituting $R^2 = Y$ and $2R\partial R = \partial Y$ in the above equations, the corresponding equations for use in the secondary cylindrical systems may be obtained with respect to the co-ordinates R and Z. In toroidal co-ordinates, the equations are

$$\begin{aligned}\frac{\partial\eta}{\partial t'} = &-\frac{1}{N_{\mathrm{str}}}\left[\frac{1}{\rho}\frac{\partial}{\partial\rho}(\rho V_\rho\eta)+\frac{1}{\rho}\frac{\partial}{\partial\phi}(V_\phi\eta)\right]\\ &+\frac{1}{\tilde{N}_R}\left[\frac{1}{\rho^2}\frac{\partial}{\partial\rho}\left(\rho^2\frac{\partial\eta}{\partial\rho}\right)-\frac{R_{00}}{R}\frac{1}{\rho}\frac{\partial\eta}{\partial\rho}-\frac{\eta}{R^2}+\frac{\cos\theta}{R\rho}\frac{\partial\eta}{\partial\phi}+\frac{1}{\rho^2}\frac{\partial^2\eta}{\partial\phi^2}\right],\end{aligned} \tag{9}$$

$$\frac{\partial^2\xi}{\partial\rho^2}+\frac{R_{00}}{R\rho}\frac{\partial\xi}{\partial\rho}-\frac{\cos\phi}{R\rho}\frac{\partial\xi}{\partial\phi}+\frac{\partial^2\xi}{\rho^2\partial\phi^2} = R\eta, \tag{10}$$

$$V_\rho = -\frac{1}{R\rho}\frac{\partial\xi}{\partial\phi}, \quad V_\phi = \frac{1}{R}\frac{\partial\xi}{\partial\rho}, \tag{11}$$

and
$$\eta = \frac{1}{\rho}\frac{\partial}{\partial \rho}(\rho V_\phi) - \frac{1}{\rho}\frac{\partial V\rho}{\partial \phi}, \tag{12}$$

where V_ρ and V_ϕ are the normalized velocity components in the ρ and ϕ directions respectively. The local co-ordinates (ρ, ϕ) are related to the primary co-ordinates (R, Z) by
$$R = R_{00} + \rho \sin\phi, \quad Z = Z_{00} + \rho\cos\phi,$$
where (R_{00}, Z_{00}) denotes the location of the local origin of the toroidal system with respect to the primary origin.

The spherical system is a special case of the general toroidal system in the limit $R_{00} \rightarrow 0$. Thus (9)–(12) also hold for the spherical system with $R_{00} = 0$, and with ρ and ϕ being appropriately referred to the local origin of the spherical system.

Flow input

The instantaneous flow rate in the system (figure 2) is taken as
$$\dot{Q}(t) = \dot{Q}_{\max}\sin(\pi t/t_s), \quad t \leqslant t_s, \tag{13}$$
where the peak systolic flow is $\dot{Q}_{\max} = \frac{1}{2}\pi Q_f/t_s$. In the numerical model of the heart valve, the following input values are used:
$$a = 1\ \text{cm}, \quad Q_f = 50\ \text{cm}^3, \quad T = \tfrac{5}{6}\ \text{s (based on 72 heartbeats per minute)}$$
and
$$t_s = \tfrac{1}{3}\ \text{s}\ (= 0{\cdot}4T).$$

Initial and boundary conditions

Initially, the flow is considered to be at rest throughout the flow field. The velocity components U, W, V_ρ and V_ϕ as well as ξ and η are therefore zero at $t' = 0$ in each co-ordinate system. In the primary and secondary cylindrical systems, the flow at the inlet and exit cross-sections is assumed to be purely axial for all times such that (see figure 3)
$$U = 0 = \partial U/\partial Z \quad \text{at} \quad Z = 0, Z_e.$$

Using a subscript w to denote values at the wall, we choose $\xi_w = 0$ arbitrarily as a reference stream-function value. Along the straight sections of the solid walls,
$$U_w = 0 = W_w, \quad \eta_w = -\partial W/\partial R \tag{14}$$
must be satisfied. Along the curved sections of the walls, including the corners,
$$(V_\rho)_w = 0 = (V_\phi)_w, \quad \eta_w = \partial V_\phi/\partial \rho \tag{15}$$
must be satisfied. Thus vorticity at the sharp corner O_2 is multi-valued, being a function of the angle ϕ of the upstream toroidal system.

The centre-line of the valve geometry is a streamline for which $\psi_0 = \dot{Q}(t)/2\pi$, and, by symmetry, $U = 0 = \partial W/\partial R$ and $\eta = 0$ at $R = 0$.

One final set of conditions must be satisfied as a consequence of the introduction of a hybrid-mesh system: at every point of the primary–secondary and secondary–secondary fluid interfaces, the values of ξ and η must match.

A complete determination of the entire flow field requires the simultaneous solution of the flow problems associated with all the co-ordinate systems, as stated above. Apart from the developing flow pattern itself, a quantity of particular interest in haemodynamic analysis is the magnitude of the shear stress τ along the solid walls. It can be shown that the wall shear is directly proportional to the wall vorticity according to the relation

$$\tau_w/\rho\langle\overline{w}\rangle^2 = -\eta_w/N_R. \tag{16}$$

Corresponding to the chosen flow inputs, the valve inlet diameter, and the physical properties of blood (density of 1·05 g/cm³, $\nu = 0{\cdot}04$ S), the following values are obtained for the characteristic velocity and the dimensionless parameters:

$$\langle\overline{w}\rangle = 47{\cdot}7\,\mathrm{cm/s},\quad N_R = 1193{\cdot}7,\quad \tilde{N}_R = 30{\cdot}0,\quad N_{\mathrm{str}} = 0{\cdot}025.$$

At peak flow, the average inlet flow velocity is 75 cm/s, which corresponds to a Reynolds number of 1875 based on the inlet radius.

4. Numerical analysis

The flow of blood through the aortic-valve geometry is highly unsteady and becomes very nonlinear as peak systolic flow rate is approached. The only promising method for treating such a flow is through finite-difference computation. The numerical procedures outlined in this paper have been described in much greater detail by Gillani (1974). The quasi-linear parabolic equations of vorticity transport, e.g. (5) or (9), and the linear elliptic equations for the stream function, e.g. (6) or (10), in each of the co-ordinate systems used for the problem are recast in finite-difference form. The parabolic equations are solved in the interior of the flow field by explicitly marching forward in time starting from the initial condition of rest. At each new time level, their solutions yield the source terms for use in the stream-function equations. These elliptic equations are then solved either by an explicit iterative method based on the optimized successive over-relaxation technique (primary and secondary spherical systems), or by a direct method based on a modified Gaussian elimination technique (secondary cylindrical and toroidal systems). In the above solutions, the matching of the values of the flow variables at the interfaces between the various sub-regions of the flow is also accomplished. The stream-function solutions in the various co-ordinate systems are then used to evaluate the velocity components according to difference approximations to (7), (11) and their counterparts in the secondary cylindrical and spherical systems. Since the secondary systems are chosen to run locally parallel to the solid walls, the wall vorticity, whose definition uses the gradient of the velocity component parallel to the wall [cf. (14) and (15)], is easily determined. Furthermore, this evaluation of the wall vorticity is quite accurate owing to the fine structure of the secondary meshes. Finally, the magnitude of the wall shear stress is calculated using (16).

For a given system of differential equations, many different sets of difference schemes can be formulated. Each set represents a different approximation. The particular choice of difference scheme and the method of its solution, as well as the choice of time interval and the finite-difference mesh, will, in general, deter-

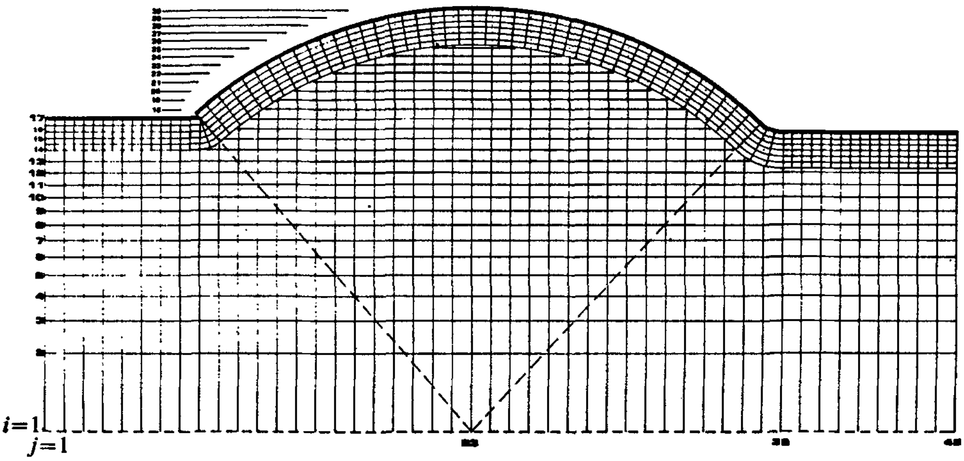

FIGURE 4. The hybrid system of finite-difference meshes. The primary mesh is shown before radial transformation.

mine the consistency, accuracy, numerical stability and convergence of the solution. The practical considerations in making these choices are mostly based on available computer time and storage.

System of finite-difference meshes

The primary emphasis in this paper is on the practical application of numerical methods to the problem of separated unsteady viscous flow through circular ducts of complex axial geometries. A central thesis of this paper is that proper treatment of the boundary-region flow is essential to the realistic simulation of the separated flow. Of particular importance is the treatment of the flow in the vicinity of the corners at the two ends of the spherical cavity. In response to these considerations, the choice of fine-mesh systems running parallel to the solid walls was made. Considerations of available computational resources led to the choice that the fine grid be restricted to the boundary region only, and that a primary and coarser grid be established in the remaining bulk of the flow region and be aligned with the central axis of flow.

The complete hybrid system of meshes occupying the primary and the secondary regions of the real flow field is shown in figure 4. In the primary region, a 30×48 mesh provides uniform spacing axially and a progressively decreasing spacing radially away from the axis. In the transformed Y, Z plane ($Y = R^2$), the mesh cells are identical squares with $\Delta Y = \Delta Z = h$. Since there exists a one-to-one correspondence between the primary nodes in the real and the transformed planes, the nodal values of η and ξ can be obtained from the solution of the transformed flow equations and then transferred directly to the corresponding nodes in the real plane. The subsequent matching of the variables along intra-system interfaces is always performed in the real geometry since all the secondary systems are defined in the real geometry. A number of primary nodes are located inside the secondary regions. Owing to the presence of the curved boundary, some of

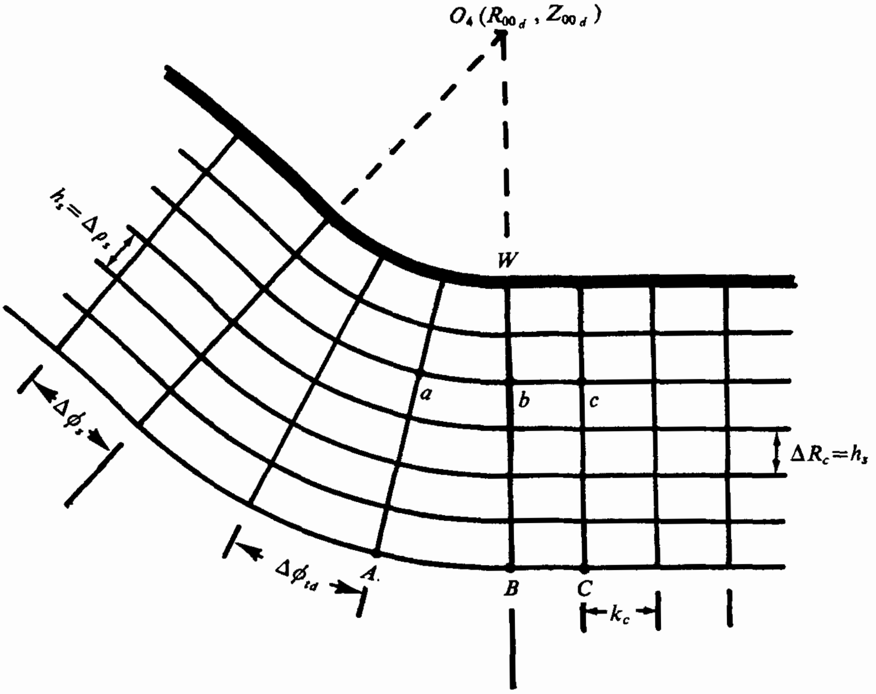

Figure 5. Close-up view of the secondary meshing around the downstream corner. The annular surface represented by the line *WbB* is a secondary–secondary interface.

these primary nodes are irregular stars, that is, their distance from the solid wall is less than the normal primary mesh spacing in at least one co-ordinate direction. These nodes require special treatment in the numerical computations, as will be described later.

The secondary grid lines run parallel and perpendicular to the solid walls. The secondary radial grid spacings, i.e. ΔR_c in the cylindrical systems and $\Delta\rho$ in the spherical and toroidal systems, are all equal and denoted by h_s (figure 5). The secondary axial grid spacing is the same in the two cylindrical systems, and is denoted by $k_c = \Delta Z_c$. The angular grid spacings are $\Delta\phi_s$ in the spherical system, and $\Delta\phi_u$ and $\Delta\phi_{td}$ in the upstream and downstream toroidal systems, respectively. The numerical values of the primary and secondary mesh spacings are chosen as

$$h = \tfrac{1}{16} = 0{\cdot}0625; \quad h_s = 0{\cdot}02, \quad k_c = \tfrac{1}{2}h = 0{\cdot}03125;$$

$$\Delta\phi_s = 2{\cdot}059^\circ, \quad \Delta\phi_{tu} = 20{\cdot}59^\circ, \quad \Delta\phi_{td} = 14{\cdot}42^\circ.$$

The choice of the time interval $\delta t'$ for an explicit scheme is generally restricted by considerations of numerical stability. Numerical instabilities may be of a static or a dynamic nature (Roach 1972*a*). In the static case, the growth of errors is monotonic and due largely to the nature of the difference scheme itself. Static stability may be attained by restricting the maximum Reynolds number based on cell size. In the dynamic case, the numerical solution oscillates about the true solution as the errors grow. Dynamic stability may be attained by restricting the size of $\delta t'$. For the vorticity-transport equation, the destabilizing effect of greatest concern is that due to the nonlinear terms of vortex-line stretching and convection. These effects are small near the solid boundaries except in the region downstream of the sharp corner, where the rates of both stretching and convection of vortex lines are substantially enhanced. The nonlinear effects are most dominant, however, in the primary region where flow divergence takes place. For this reason, the restriction on $\delta t'$ is based on a stability criterion obtained for the primary system. Furthermore, corresponding to the choice of $\delta t'$ in this manner, it is necessary that the angular spacing $\Delta\phi_{tu}$ satisfy some appropriate condition to ensure stability in the region surrounding the sharp corner. It has been suggested by Gillani (1974), on the basis of trial and error, that $\Delta\phi_{tu}$ be chosen such that the average circumferential grid spacing in the secondary corner region be at least half of the corresponding grid spacings parallel to the wall in the neighbouring secondary regions. This condition is satisfied by the chosen value of $\Delta\phi_{tu}$.

Finite-difference equations

Finite-difference equations are presented only for the transformed primary system. The corresponding equations in the secondary meshes are of an analogous form.

Accuracy and convergence are the principal goals in computational simulation of flow dynamics. At least for linear equations, a consistent finite-difference formulation and its stable solution are sufficient conditions for convergence, given arbitrary well-behaved initial conditions (Richtmeyer & Morton 1967). For the linear case, convergence will not depend on boundary conditions (O'Brien, Hyman & Kaplan 1951). For the quasi-linear case of the vorticity-transport equation, a mild strengthening of the stability criterion at a primary interior node based on local linearization of the equation is found to be sufficient to ensure a stable solution. Accuracy may not always improve with a higher-order difference approximation. It is a matter of general experience, for example, that formulae claiming high orders of accuracy, e.g. $O([\delta t]^4)$, are often quite disappointing in practice (Richtmeyer & Morton 1967). One exception is the successful application of a fourth-order scheme in a plane two-dimensional flow field by Fromm (1969) in an attempt to curtail numerical-dispersion errors, which can be serious at high Reynolds number. Second-order differencing of the linear as well as the nonlinear terms of the vorticity-transport equation leads to dispersion errors which manifest themselves as spatial oscillations where high local gradients occur at high Reynolds number. Replacing the second-order differencing of the nonlinear terms by first-order upwind differencing (Courant, Isaacson & Rees 1952) aids numerical stability by the introduction of artificial numerical damping, but at the same time reduces the accuracy. For flows of sufficiently limited Reynolds number, such a scheme using centred differences in all except the nonlinear terms generally provides a stable solution of reasonable accuracy. The use of upwind differencing for the nonlinear transport terms possesses the additional attribute that the physical transport of vorticity is maintained in the local direction of flow.

If	Then
$U^+ \geqslant 0$ and $U^- \geqslant 0$	$U_G = U^+$ $(U\eta)_H = U^- \eta_{i-1,j}$
$U^+ \geqslant 0$ and $U^- < 0$	$U_G = U^+ - U^-$ $(U\eta)_H = 0$
$U^+ < 0$ and $U^- \geqslant 0$	$U_G = 0$ $(U\eta)_H = -U^+\eta_{i+1,j} + U^-\eta_{i-1,j}$
$U^+ < 0$ and $U^- < 0$	$U_G = -U^-$ $(U\eta)_H = -U^+\eta_{i+1,j}$
$W^+ \geqslant 0$ and $W^- \geqslant 0$	$W_G = W^+$ $(W\eta)_H = W^-\eta_{i,j-1}$
$W^+ \geqslant 0$ and $W^- < 0$	$W_G = W^+ - W^-$ $(W\eta)_H = 0$
$W^+ < 0$ and $W^- \geqslant 0$	$W_G = 0$ $(W\eta)_H = -W^+\eta_{i,j+1} + W^-\eta_{i,j-1}$
$W^+ < 0$ and $W^- < 0$	$W_G = -W^-$ $(W\eta)_H = W^+\eta_{i,j+1}$

TABLE 1. The definitions of the second upwind difference parameters. The definitions are based on the signs of $U^\pm$ and $W^\pm$, where $U^\pm = \frac{1}{2}(U_{ij} + U_{i\pm1,j})$ and $W^\pm = \frac{1}{2}(W_{ij} + W_{i,j\pm1})$.

In the difference formulation, vorticity at the node (Y_i, Z_j) in the primary system at time $n\delta t'$ is denoted by η^n_{ij}. Other variables are similarly defined. The difference scheme chosen to approximate (5) uses centred time differencing, centred space differencing for the diffusion terms, and second upwind differencing (Roache 1972*a*) or 'donor-cell' differencing (Gentry, Martin & Daly 1966) of the nonlinear transport terms. Furthermore, at the node (i, j) where the difference equation is applied, the following Dufort–Frankel leapfrog substitution (Dufort & Frankel 1953; Fromm 1963) is made for η^n_{ij} in the diffusion terms as well as in the nonlinear terms:

$$\eta^n_{ij} \approx \tfrac{1}{2}(\eta^{n+1}_{ij} + \eta^{n-1}_{ij}).$$

The resulting difference formula is

$$\eta^{n+1}_{ij} \approx (1-\alpha G_{ij})(1+\alpha G_{ij})^{-1}\eta^{n-1}_{ij} + 2\alpha(1+\alpha G_{ij})^{-1}\{hN_R[2R_i(U\eta)_H + (W\eta)_H] \\ + 4Y_i(\eta_{i+1,j} + \eta_{i-1,j}) + 2h(\eta_{i+1,j} - \eta_{i-1,j}) + \eta_{i,j+1} + \eta_{i,j-1}\}, \quad (17)$$

where $$\alpha \equiv \delta t'/h^2\tilde{N}_R,$$

and $$G_{ij} \equiv 2(1+4Y_i) + h^2/Y_i + hN_R(2R_i U_G + W_G).$$

The quantitites U_G, W_G, $(U\eta)_H$ and $(W\eta)_H$ are defined in table 1. The superscript is assumed to be n, by default, whenever it is absent.

The enhanced stability of upwind differencing over central differencing of the transport terms is a result of the introduction of an artificial viscosity term in the numerical procedure (Roache 1972*b*). Denoting the actual viscous diffusion term in (5) as D_v and the artificial diffusion term effectively introduced by the numerical procedure as D'_v, Gillani (1974) has shown that

$$\frac{D'_v}{D_v} \approx \tfrac{1}{2}hN_R \frac{2R|U|\eta_{YY} + |W|\eta_{ZZ}}{4Y\eta_{YY} + 4\eta_Y - (\eta/Y) + \eta_{ZZ}}, \quad (18)$$

where the subscripts Y and Z denote derivatives with respect to those co-ordinates. The ratio of artificial to real diffusion is a measure of the size of the numerical damping error. The numerical damping error is proportional to the mean systolic cell Reynolds number hN_R, and it grows as the flow accelerates. It is not possible to obtain *a priori* estimates of this error.

Neutral static stability is ensured by the use of the Dufort–Frankel scheme. In the primary system, the dynamic stability criterion which restricts the size of $\delta t'$ is (Gillani 1974)

$$\delta t' < h^2 \tilde{N}_R / [2(1+4Y_i) + (h^2/Y_i) + hN_R(2R_i|U_{ij}| + |W_{ij}|)]. \tag{19}$$

This stability restriction on the choce of $\delta t'$ becomes progressively more stringent as the flow accelerates, and is predominantly dictated by the magnitude of the flow term $2R_i|U_{ij}| + |W_{ij}|$. This term attains its maximum value where there is substantial radial flow, for example where the main flow diverges into the cavity and again where it converges back into the lumen. A pessimistic bound on $\delta t'$ is obtained by taking $|U_{ij}| = |W_{ij}| = \frac{1}{2}\overline{W}_{in}$ along the line $R_i = 1 = Y_i$, where $\overline{W}_{in}$ represents the instantaneous value of the axial flow velocity averaged over the inlet cross-section. In the computations, $\delta t'$ is decreased in steps as the flow accelerates, from an initial value of 0·0015 to a final value of 0·0007.

The difference scheme described in (17) is a three-time-level formula characteristic of the Dufort–Frankel method. It requires the values of η^0_{ij} as well as η^1_{ij} at all internal nodes in the start-up procedure. The initial condition of rest specifies η_{ij} only at $t' = 0$. During the first time interval ($\delta t' = 0{\cdot}0015$), a very thin boundary layer of finite vorticity will line the solid walls. The dimensionless thickness of this layer may be estimated as $(\nu\delta t)^{\frac{1}{2}}/a = (\delta t'/\tilde{N}_R)^{\frac{1}{2}} = 0{\cdot}007$. Since this distance of vorticity diffusion is much less than the smallest mesh spacing ($h_s = 0{\cdot}02$), it is safe to take $\eta^1_{ij} = 0$ at all primary and secondary interior nodes.

The difference formulation of the primary stream-function equation (6) at interior nodes is obtained using centred space differences, and is expressed in the following form appropriate for iterative solution by successive over-relaxation (Young 1954):

$$\xi^{(k+1)}_{ij} = \xi^{(k)}_{ij} + \tfrac{1}{2}\Omega_0(1+4Y_i)^{-1}[4Y_i(\xi^{(k)}_{i+1,j} + \xi^{(k+1)}_{i-1,j}) - 2(1+4Y_i)\xi^{(k)}_{ij} + \xi^{(k)}_{i,j+1} + \xi^{(k+1)}_{i,j-1} - h^2R_i\eta^{n+1}_{ij}]. \tag{20}$$

The superscripts to the stream function ξ denote the iteration number, and Ω_0 is the over-relaxation parameter. The term including η^{n+1}_{ij} is the source term made available at each node following the solution for the vorticity at a new time level. The optimum value of the parameter Ω_0 giving fastest convergence was obtained by numerical experimentation. For the primary system, $\Omega_0 = 1{\cdot}758$ is optimum.

At the beginning of the iteration procedure for each new time level, the starting solution $\xi^{(0)}_{ij}$ must be provided. The following rule for generating this starting solution from the solution at the previous time level is found to result in very rapid convergence:

$$(\xi^{(0)}_{ij})^{n+1} = (\xi_{ij})^n \dot{Q}^{n+1}/\dot{Q}^n.$$

Each iteration procedure is interrupted every ten sweeps of the field to check for convergence. The procedure is terminated when the desired level of convergence is attained or when the limit of convergence imposed by single-precision round-off errors is reached.

The difference equations corresponding to (7) and (8) are

$$U_{i,\,j+\frac{1}{2}} \approx (\xi_{i,\,j+1}-\xi_{ij})/hR_i, \quad W_{i+\frac{1}{2},\,j} \approx 2(\xi_{ij}-\xi_{i+1,\,j})/h \tag{21}$$

and

$$\eta_{ij} = h^{-1}[(U_{i,\,j+\frac{1}{2}}-U_{i,\,j-\frac{1}{2}})-2R_i(W_{i+\frac{1}{2},\,j}-W_{i-\frac{1}{2},\,j})]. \tag{22}$$

Primary nodes within secondary regions are given special treatment. Specific finite-difference formulations are derived for the irregular stars. Vorticity at these primary nodes is first evaluated using the primary difference solution. At a later stage, when the vorticity solution at the same time level is completed for the interior as well as the boundary nodes in the secondary meshes, vorticity values at the primary nodes concerned are adjusted to match the more accurate secondary solution. This adjustment is based on a four-point area interpolation (Gillani 1974) using values at the secondary nodes of the cell containing the primary node.

Boundary conditions

The axis of symmetry is a streamline on which the values of ξ and η are

$$\xi_0^n = \tfrac{1}{4}\pi \sin(\tfrac{5}{2}\pi n\delta t'), \quad \eta_0^n = 0.$$

At the inlet cross-section, the flow is axial and $\xi_{ij} = \xi_{i,\,j-1}$. Inlet vorticity is computed according to its definition (22) *after* the flow solution is obtained at each new time level. At the exit, the flow emerges axially and continues to be axial. Hence

$$\xi_{i,\,j+1} = \xi_{i,\,j}, \quad \eta_{i,\,j+1} = \eta_{ij}.$$

Similar boundary conditions hold at the inlet and at the exit in the secondary cylindrical systems.

Along the solid walls, in all systems, $\xi_w = 0$. The wall vorticity is computed after the solution for ξ is completed in all systems. Using (14) along the straight walls and (15) along the curved walls and at the sharp corner, invoking the no-slip condition, we have

$$\eta_{i_w,\,j} = 2\xi_{i_w-1,\,j}/h_s^2 R_{i_w-\frac{1}{2},\,j}$$

in the secondary cylindrical and spherical systems, and

$$\eta_{i_w,\,j} = 2\xi_{i_w+1,\,j}/h_s^2 R_{i_w+\frac{1}{2},\,j}$$

in the toroidal systems around the corners. R_{ij} represents the radial distance from the axis of symmetry to the secondary node (i,j). According to the last equation, the vorticity is multi-valued at the sharp corner depending on which particular secondary radial ray of the local polar co-ordinate system is considered. Roache (1972*a*) considered seven different treatments of the wall vorticity at a sharp corner and concluded that "good accuracy near a sharp convex corner, and a fully satisfactory resolution of the question of separation in the vicinity of the sharp corner, will be achieved only by a local solution in polar co-ordinates centered on the sharp corner". Our experience bears out this remark. Following the evaluation of wall vorticity at secondary nodes on the walls, simple linear interpolation between these values is used to determine wall-vorticity values at the points of intersection of the primary mesh lines with the wall.

The values of η and ξ at secondary nodes adjacent to the primary interior are obtained from the primary solution by a four-point area interpolation using the four nodes of the primary cell within which the secondary node in question is located (Gillani 1974). All secondary–secondary interfaces are in the vicinity of the corners leading into and out of the cavity. Figure 5 illustrates the manner in which η and ξ are evaluated along these interfaces, with specific reference to the interface between the secondary downstream toroidal and cylindrical systems. At the point b along the interface WB, η_b is computed by simple linear interpolation between the values of η_a and η_c based on the assumption that vorticity changes uniformly from a to b to c along the grid lines parallel to the wall. ξ_b, on the other hand, is computed using the assumption that

$$(\xi_b-\xi_w)/(\xi_B-\xi_w) \approx (\xi_a-\xi_w)/(\xi_A-\xi_w).$$

Thus, since $\xi_w = 0$, we have $\xi_b \approx (\xi_B/\xi_A)\,\xi_a$. This extrapolation from a to b is in the direction of flow.

Motion of the leaflet

The closed position of the leaflet is shown in figure 1, and corresponds to the condition at $t' = 0$. The total length of the leaflet is about $1{\cdot}5a$. At closure, nearly a quarter of this length is along the co-apting leaflet surfaces at the axis. In the analysis, the leaflet is assumed to behave like a thin, neutrally buoyant membrane which offers no resistance to fluid flow at early times in the acceleration phase. Leaflet motion is analysed only as long as such an assumption is valid. The leaflet contour is approximated by thirteen freely hinged rigid 'rods' of equal length. The first of these rods is permanently hinged at one end of the valve ring at the sharp corner leading into the spherical cavity. The last three rods are initially coincident with the valve axis. Each joint along the leaflet contour is allowed to move as a local fluid particle except for the additional constraints that the chain of rods must remain hinged at the valve base and that each rod must remain the same length. The corresponding formulae for evaluating the displacement of each joint during each time interval of the finite-difference scheme have been used as derived by Gillani (1974).

5. Experimental investigation

The primary objective of the experimental investigation was a qualitative visualization of the unsteady development of the laminar separation wake in the spherical cavity of an axisymmetric acrylic model. The experimental apparatus is shown in figure 6. The spherical cavity is contained within the axisymmetric test section, the internal surface of which is polished. Nearly sharp corners exist at both ends of the cavity, and the inlet and exit radii of the duct are equal (1·91 cm). The radius of the cavity is 1·37 times greater. The left ventricle is modelled by a pump cylinder with a moving piston driven by a cam designed to

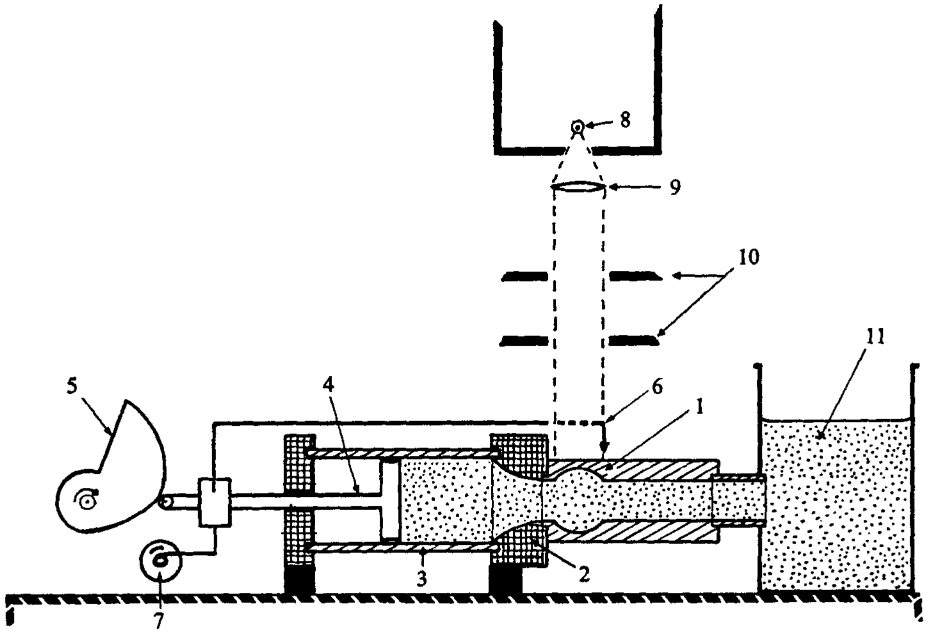

FIGURE 6. Schematic drawing of experimental set-up. 1, test section with spherical cavity; 2, inlet tract nozzle; 3, pump cylinder; 4, piston; 5, cam; 6, pointer (position indicator); 7, tachometer generator; 8, light source; 9, collimator lens; 10, parallel slits; 11, fluid with suspended particles.

deliver a forward sinusoidal pulse. The displacement of the piston is equal to that of a metal pointer (position indicator) which is attached to the piston assembly and which moves above the test section. The rate of displacement of the piston is monitored by a tachometer generator, and is recorded on a strip-chart recorder. A nozzle connecting the pump chamber and the test section represents the inlet tract to the valve.

The fluid used in the model study was a mixture of water, glycerin and pluracol (a thick, highly viscous, water-soluble liquid) in the ratio 100·0:19·0:5·3. Suspended very homogeneously in this liquid mixture were spherical plastic beads ranging in diameter from 400 to 500 μm. The specific gravity of the liquid and the beads was equal to that of blood (1·05). The kinematic viscosity of the liquid mixture was 0·098 S at 24 °C.

An optical system consisting of a high-intensity mercury arc lamp (light source), a collimator lens and two narrow parallel slits provides illumination of the vertical plane through the axis of the test section. Photographs of the suspended plastic beads moving through the cavity in this vertical plane are taken by a camera mounted in front of the apparatus, level with the axis of symmetry. Only the tip of the position indicator moves in the illuminated plane, and casts a shadow below its position at the time the picture is taken.

An exact matching of the similarity parameter $\tilde{N}_R$ is achieved in the numerical and experimental models by adjusting the rotation speed of the cam. The net

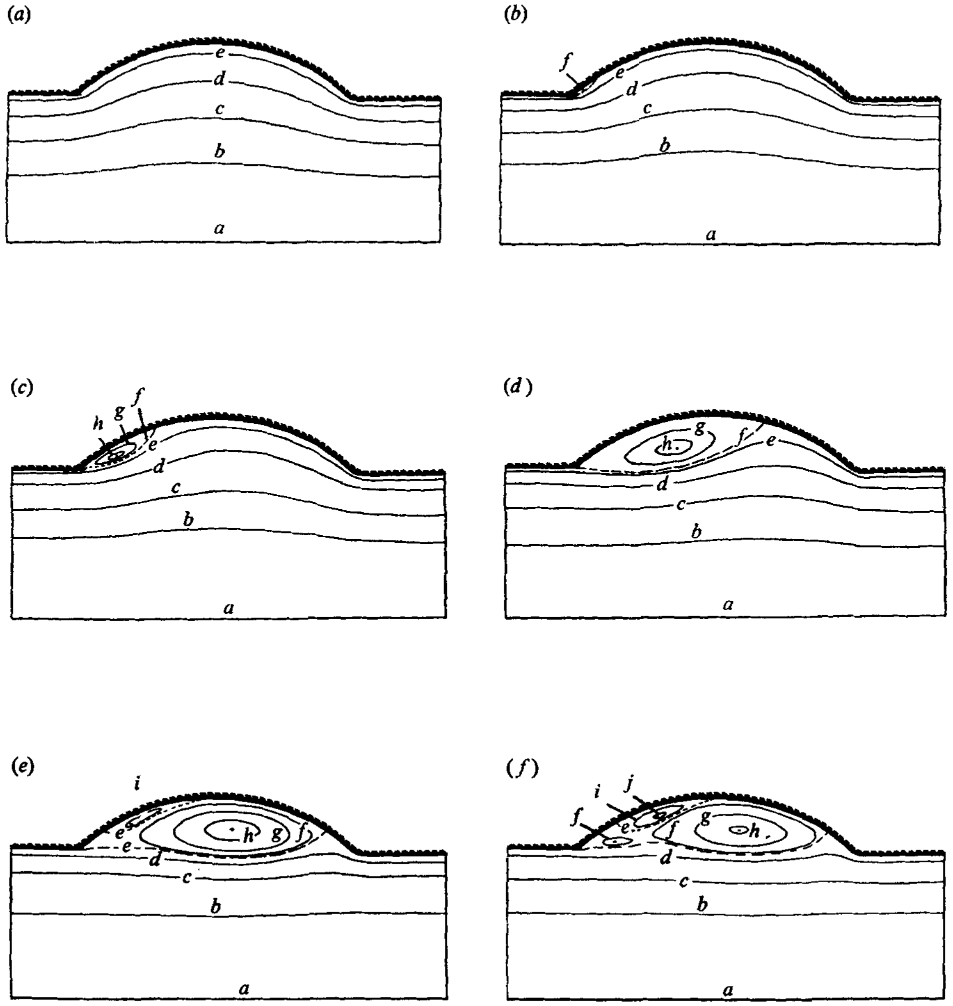

FIGURE 7. Streamlines calculated from the numerical solution. The values of t' for (a)–(f) are 0·015, 0·045, 0·069, 0·120, 0·174 and 0·1836. For each streamline plot, the values of ξ can be listed in the alphabetical order in which the streamlines themselves are labelled. (a) $\xi_a, \ldots, \xi_e$ = 0·092, 0·075, 0·050, 0·025, 0·005. (b) $\xi_a, \ldots, \xi_f$ = 0·272, 0·200, 0·125, 0·050, 0·005, 0·000. (c) $\xi_a, \ldots, \xi_h$ = 0·405, 0·300, 0·200, 0·075, 0·010, 0·000, −0·002, −0·005. (d) $\xi_a, \ldots, \xi_h$ = 0·635, 0·500, 0·300, 0·125, 0·020, 0·000, −0·040, −0·070. (e) $\xi_a, \ldots, \xi_i$ = 0·769, 0·500, 0·200, 0·050, 0·000, −0·010, −0·050, −0·100, −0·005. (f) $\xi_a, \ldots, \xi_j$ = 0·779, 0·500, 0·250, 0·050, 0·000, −0·005, −0·050, −0·090, 0·002, 0·005.

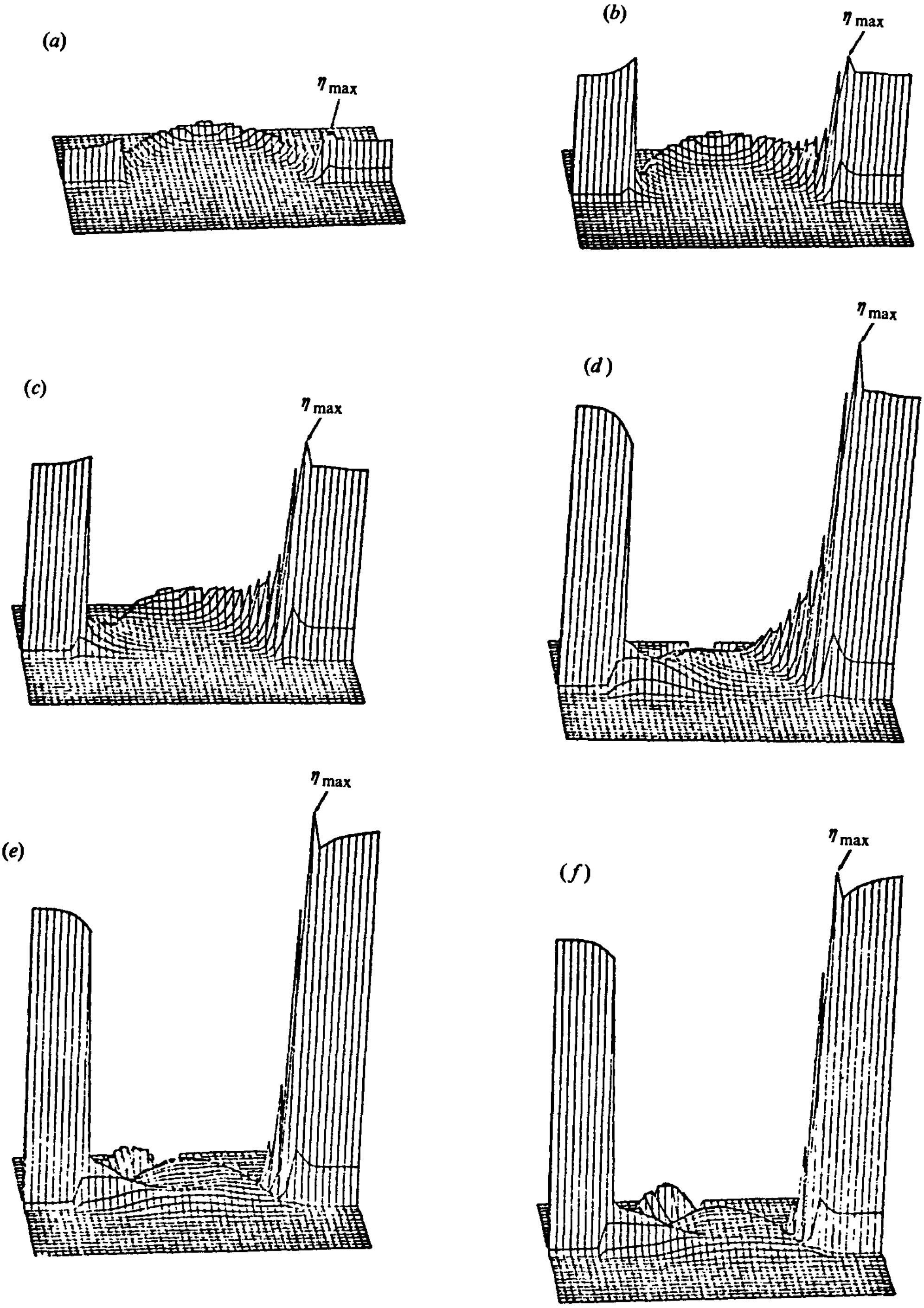

FIGURE 8. Vorticity calculated from the numerical solution. (Three-dimensional plots are computer-generated.) The values of t' for (*a*)–(*f*) are 0·015, 0·045, 0·069, 0·120, 0·1740, 0·1836, and the maximum values of η are 16·6, 50·2, 80·9, 139·4, 151·4, 141·0.

forward flow in the experimental model is 320 cm^3, giving $N_R = 1096$. This compares with the corresponding value of 1194 in the numerical model. The flows in the two models may thus be expected to be substantially similar.

6. Results and discussion

Numerical results

Computations were carried out for 196 time intervals comprising the accelerating-flow phase from rest to peak systole ($t' = 0{\cdot}2$). Streamlines of flow for selected time levels are shown in figure 7. Three-dimensional computer-generated plots of vorticity at the corresponding times are shown in figure 8. Two distinct chronological phases of flow are identified. Phase 1 lasts for values of t' between zero and approximately 0·15, and is characterized primarily by the gradual development and strengthening of a well-defined annular vortex within the spherical cavity. Phase 2 occupies the remaining quarter of the time range studied. During phase 2, the appearance and growth of a secondary vortex pattern causes a gradual weakening of the primary vortex. The numerical solution remains stable throughout both phases.

In the early stages of acceleration ($t' = 0{\cdot}015$), the flow is almost potential flow and closely follows the contour of the solid boundary. A small amount of vorticity is seen lining this boundary. In the absence of any significant stretching or convection of vorticity at this early time, a striking degree of symmetry is observed in the flow between the upstream and downstream sides of the cavity. This symmetry soon breaks down following flow separation, which is first detected at $t' = 0{\cdot}039$. The separation occurs at or immediately behind the sharp convex corner, and the separation streamline delineates a small annular eddy ($t' = 0{\cdot}045$). Along this streamline, $\xi = 0$.

As the flow accelerates, more energy is fed into the captive vortex across the free shear layer lining the major portion of the separation streamline. Consequently, the vortex grows in size, continuously pushing the stagnation point at reattachment further downstream ($t' = 0{\cdot}069$–$0{\cdot}120$). Progressively, the earlier symmetry of the flow within the cavity is replaced by the growing vortex on the upstream side and a relative crowding of the streamlines on the downstream side. Vorticity and wall shear stress grow conspicuously along the straight edges of the solid wall near the inlet and exit sections. At early times, the bending of the flow around the sharp corner into the cavity results in a local peak of wall vorticity at the sharp corner ($t' = 0{\cdot}045$). However, the gradual growth of a boundary layer along the straight wall on the inlet side combines with the general reshaping of the main flow, which accompanies the growth of the eddy, to cause a slightly divergent flow near the inlet wall. As a result, there is a small decrease in wall vorticity as the sharp corner is approached from the upstream side ($t' \geqslant 0{\cdot}120$). Behind the sharp corner, the flow is reversed along the sinus wall and the wall vorticity is negative. Thus there is a discontinuous drop in the vorticity around the sharp corner, itself a point of singularity.

Convective transport of vorticity from the upstream boundary-layer region near the sharp corner is seen to maintain a ridge of high vorticity along the free shear layer accompanying the separation streamline. Some of this vorticity then diffuses towards the vortex core and helps to sustain the circulation. Obviously, the shear layer of concentrated vorticity cannot extend all the way to the reattachment point, because the condition of zero shear at the stagnation point must be satisfied. Thus, as the stagnation point is approached, the streamlines on either side of the separation streamline diverge from it and, when the stagnation point is reached, proceed in opposite directions. A region of low shear therefore exists in the vicinity of the reattachment, and wall vorticity and shear change sign as the stagnation point is passed. Past the stagnation point, the reversed streamline follows the sinus wall back towards the separation point. The streamline on the side of the main flow, on the other hand, continues forward past the reattachment point, turns towards the lumen and converges towards the smooth downstream corner. A region of increasing wall shear and wall vorticity accompanies it to the corner, where the wall experiences the highest shear of the flow. At $t' \approx 0{\cdot}15$, the vortex attains its maximum size and strength and occupies much of the cavity.

According to the numerical solution, very conspicuous secondary developments occur during phase 2 of the flow ($t' > 0{\cdot}15$). As the reversed flow of the recirculating primary vortex approaches the upstream corner, it diverges from the curved wall and experiences an adverse pressure gradient and a growing boundary layer. At $t' = 0{\cdot}156$, this reversed flow itself separates from the wall, giving rise to a secondary vortex whose circulation is clockwise, which is opposite to that of the primary vortex ($t' = 0{\cdot}1740$).

The secondary vortex then grows as vorticity and energy are transferred to it from the parent vortex by molecular diffusion. A portion of the energy which the primary vortex derives from the main stream thus becomes diverted to the secondary vortex. At this stage in the flow cycle, however, the rate of increase of the kinetic energy of the main stream is small, and the amount of energy transferred from the main flow into the circulating flow of the cavity is inadequate to sustain the growth of both the primary and the secondary vortices. Consequently, the growth of the secondary vortex is at the expense of the primary vortex.

The secondary vortex starts only a short distance behind the sharp corner. As it grows, however, it shifts away from the sharp corner and deeper into the cavity. In so doing, it pushes the primary vortex and changes its orientation from an inclined position ($t' = 0{\cdot}120$) to a position more parallel to the flow axis ($t' = 0{\cdot}1740$). More significantly, however, the primary vortex core is pushed from the cavity centre increasingly towards the downstream corner. Such a relocation of the main eddy was observed in the studies of aortic-valve models by Bellhouse & Talbot (1969) at the corresponding time in the flow cycle. With the shift of the vortices to the right, a region of relative stasis consisting of a narrow tail-end of the primary vortex remains in the portion of the cavity immediately behind the sharp corner. Upon further transport of vorticity into this region from the upstream boundary layer, a split develops in the main vortex which results in the birth of a small trailing vortex just behind the sharp corner ($t' = 0{\cdot}1836$). This new vortex has the same anticlockwise rotation as the primary vortex.

The appearance of the new vortex at the base of the cavity occurs at $t' = 0{\cdot}18$. In the final moments of the acceleration phase, the new vortex grows as a member

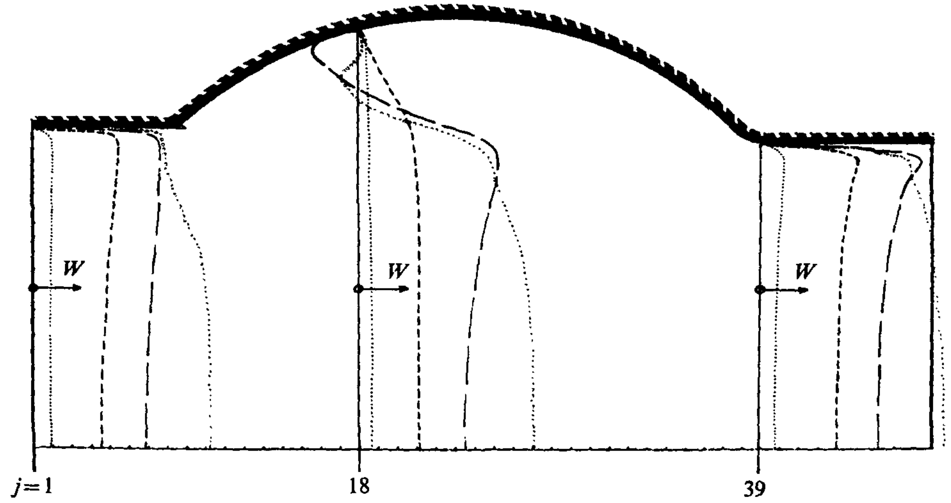

FIGURE 9. Selected radial profiles of axial velocity component W from the numerical solution. ···, $t' = 0{\cdot}015$; - - - -, 0·069; – – –, 0·120; oooo, 0·200.

of the split pair by directly feeding upon the main flow while its older sibling cotinues to degenerate, and with it also the parasitic secondary vortex. The flow in much of the core region of the valve appears to remain almost exactly axial throughout the acceleration phase, particularly at higher flow rates. This result is consistent with the observations of Bellhouse & Talbot (1969) and of Bellhouse (1969).

The appearance of a secondary vortex after the separation of the reversed flow itself has been observed by Thoman & Szewczyk (1969), Son & Hanratty (1969), Honji & Taneda (1969) and Collins & Dennis (1973) for impulsively generated or uniformly accelerated flows over a cylinder, by Rimon (1969) for time-dependent flow over a sphere, by Fromm (1969) for flow through a diffuser, and by Honji (1975) for the starting flow down a step. According to Thoman & Szewczyk, "the secondary vortex at first grows in size and splits the main vortex into two parts to form a second secondary vortex. The initial secondary vortex then moves to a higher angle and diminishes in size."

The numerical solution yields very clearly the course and shape of the separation streamline. Owing to the use of the fine secondary meshes, the locations of the primary and secondary reattachment points are determined quite accurately, since by definition η_w and τ_w must be zero there. The location of the primary separation point is always shown to coincide with the sharp corner even though its precise location cannot be determined. For t' approximately less than 0·1, the separation streamline starts out concave to the main flow and the separation point during that time may be slightly to the back of the corner. After that time, location of the separation actually at the corner does appear to be the case. After the birth of the primary vortex, its reattachment length along the curved wall increases linearly with the instantaneous Reynolds number at the inlet until the secondary vortex appears. Subsequently, its forward progress slows down and the stagnation point actually recedes after the birth of the split pair.

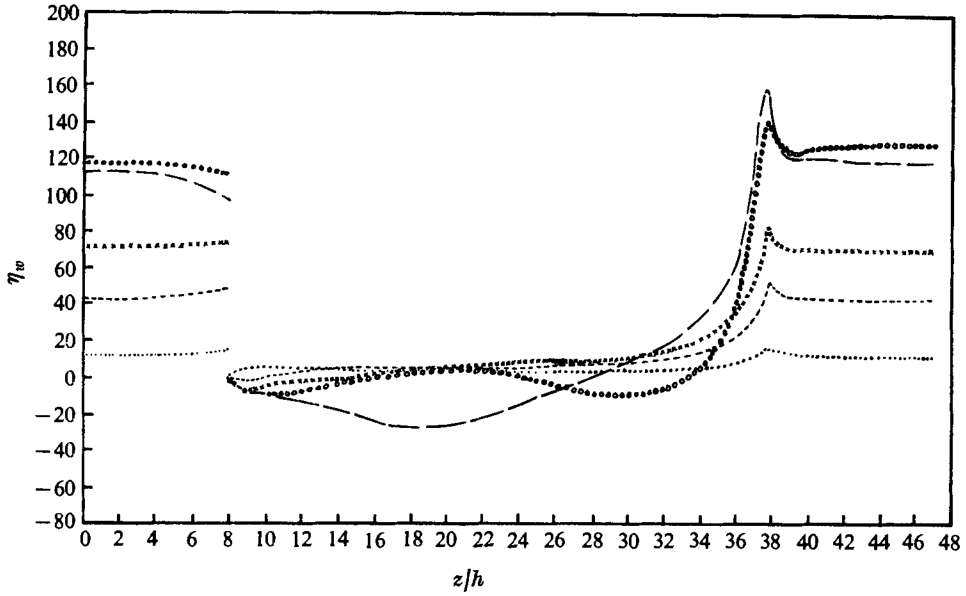

Figure 10. Wall vorticity distribution at selected times from the numerical solution. ···, $t' = 0{\cdot}015$; - - - -, 0·45; × × × ×, 0·069; ——, 0·120; oooo, 0·200. The sharp corner is located at $z/h = 8$, while the smooth corner is at $z/h = 37$.

A similar linear rate of translation of the stagnation point with increasing flow Reynolds number during a purely laminar flow regime has previously been observed in the case of the separation wake behind an abrupt expansion in a circular conduit (Macagno & Hung 1967; Back & Roschke 1972). The retreat of the reattachment point with increasing flow in an intermediate range of Reynolds number has also been observed experimentally in other separation flows (Back & Roschke 1972; Meisner & Rushmer 1963). Such a reversal is believed to indicate the beginning of laminar shear instabilities and a slow transition to turbulence (Back & Roschke 1972). Coincident with the retreat of the stagnation point, the split in the primary vortex continues and the primary separation streamline takes an increasingly wavy course. Also, for the first time, inflexions appear in the velocity profiles. Figure 9 shows radial profiles of the axial velocity component W at the inlet and exit cross-sections and at a cross-section through the centre of the cavity. The profiles corresponding to $t' = 0{\cdot}200$ at all three sections are inflected in the interior of the flow. According to the so-called point-of-inflexion criterion of Rayleigh (1913), an inflected velocity profile is a necessary condition for the occurrence of instability. Tollmien (1936) later succeeded in showing that it also constitutes a sufficient condition for the amplification of disturbances. The simultaneous occurrence of the splitting of the primary vortex, the increasingly wavy course of the separation streamline, the retreating of the primary reattachment point, and the inflecting of the velocity profiles all indicate the onset of an instability in the flow during the final moments of the acceleration phase. In figure 9, the developing velocity profiles at cross-sections of the straight portions of the duct also exhibit the familiar peaking of the

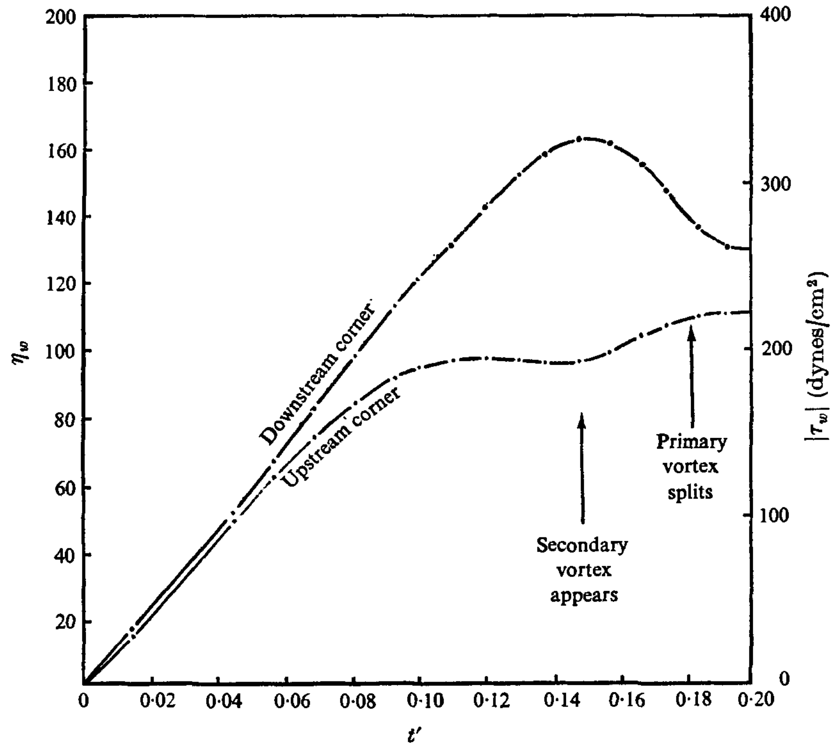

FIGURE 11. Unsteady wall vorticity η_w and wall shear stress τ_w at the corners of the spherical cavity from the numerical solution.

velocity near the wall, a characteristic of pulsatile flow in arteries. The profiles at the section through the cavity indicate regions of reversed flows of the primary vortex ($t' = 0{\cdot}120$) and also of the secondary vortex ($t' = 0{\cdot}200$).

Figure 10 shows the distribution of vorticity along the solid wall at five time levels during the acceleration phase. The discontinuity of vorticity at the sharp upstream corner and the sharp peak of vorticity at the smoothed downstream corner are the most obvious features. Vorticity and shear-stress behaviour at the two corners during the acceleration phase are highlighted in figure 11. The highest wall shear stress is attained at the downstream corner just prior to the appearance of the secondary vortex. Assuming this maximum level of shear stress of about 325 dynes/cm^2 to be an estimate of the peak shear experienced by the endothelial layer of a normal aortic valve during each heart beat, it may be concluded that, under normal physiological conditions, shear stress is insufficient to cause significant endothelial damage. Studies of endothelial damage due to high shear have shown that marked deterioration of the endothelial surface occurs when it is exposed to shear stress in excess of 380 ± 85 dynes/cm^2 for periods of about one hour (Fry 1968).

The results of computations of the motion of the meridional section of the leaflet during early systole are shown in figure 12. During early flow acceleration, the leaflet is pushed forwards and upwards. The co-aption length at the axis decreases gradually until the leaflet finally lifts off the axis at $t' = 0{\cdot}036$. Near that

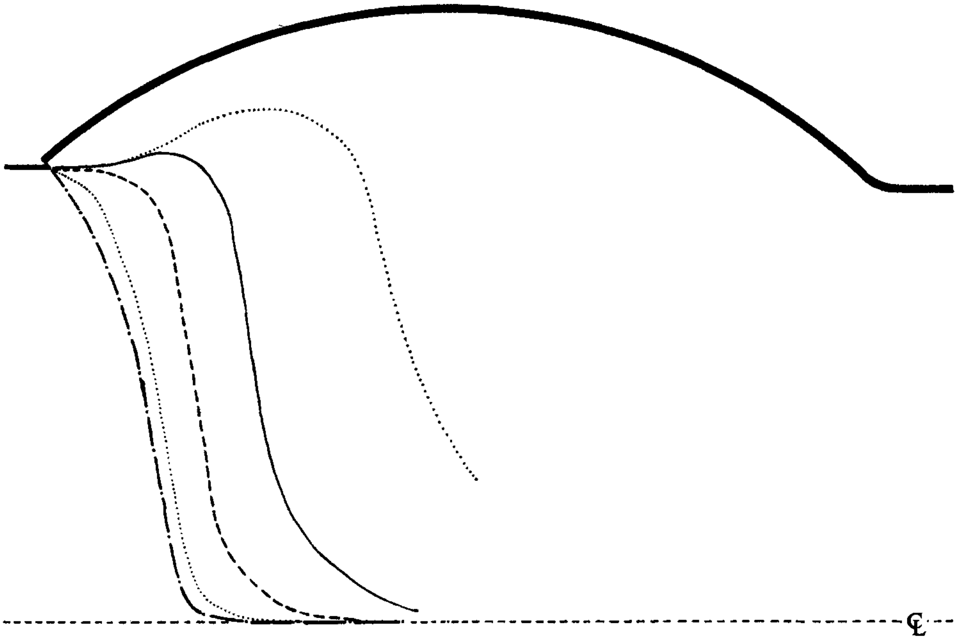

FIGURE 12. Valve-leaflet motion during early systole. —·—, $t' = 0$; ···, $t' = 0{\cdot}015$; - - -, $t' = 0{\cdot}030$; —, $t' = 0{\cdot}045$.

time, the base of the leaflet just becomes level with the upstream aortic wall. The present analysis of leaflet motion is judged to be a valid simulation of the real case only up to about $t' = 0{\cdot}045$. In the real valve, each of the three leaflets is firmly attached to the valve ring as well as to the sinus walls. The constraints on leaflet motion are three-dimensional and the assumption of an axisymmetric leaflet is no longer valid. Also, as the supporting structure of the leaflets restricts their free motion, the assumption of negligible impedance to the flow becomes increasingly questionable.

Validity of the numerical results

The solution obtained is numerically stable and convergent. The size of the truncation error is determined largely by the numerical damping arising from the upwind differencing of the nonlinear terms of the vorticity-transport equation. The second upwind differencing is of a quasi-second-order accuracy. The ratio of the artificial and real diffusion terms as given by (18) may be expected to provide the best possible estimate of the numerical damping error, which is most serious near peak-flow conditions. Applying (18) to the numerical solution at $t' = 0{\cdot}1740$ in the region outside the secondary meshes, i.e. in the valve lumen and in the middle of the spherical cavity, it is seen that D'_v/D_v is less than $0{\cdot}1$ at all such primary nodes. Equation (18) applies only to the primary mesh. In the secondary meshes, the accuracy may be expected to be higher because the cell Reynolds number is smaller, because the size of the real diffusion is highest in the secondary regions, and because both velocity components are generally smaller in the secondary regions.

Comparison of numerical and experimental results

In the experiment, the duration of the acceleration to peak flow was only 0·25 s ($t' = 0{\cdot}2$). In such a short time, a clear photographic resolution of both chronological phases of flow could not be achieved. However, photographs made over the range of phase 1 ($t' \leqslant 0{\cdot}15$) clearly reveal the development of the primary vortex in the spherical cavity of the experimental model.

Figure 13 (plate 1) shows a comparison between the flow pattern obtained in the numerical solution at $t' = 0{\cdot}120$ and that revealed by a photograph made in the shutter-open time corresponding to the period $t' = 0{\cdot}120$ to 0·133. The starting time and the exposure time of the photograph are estimated directly from the location and length of the streak marked by the motion of the position indicator seen near the top of the photograph. The exposure time estimated in this manner agrees with the setting of $\frac{1}{60}$ s on the camera. A metal wire bent in the shape of the valve leaflet contours in closed position is also seen in the photograph. This wire frame lies in the vertical illuminated plane through the valve centre-line and provides a convenient object upon which to focus the camera.

The photograph is marred slightly in the cavity region by the interfering presence of bright spots superimposed upon the flow pattern revealed in the background. The bright spots correspond to particles which do not coincide exactly with the illuminated central plane of flow. The general outline of the flow pattern is defined sufficiently well to show the vortex and the course of the separation streamline in the cavity. The size and orientation of the vortex, the location of the reattachment point, and the shaping of the streamlines of the main flow by the existence of the vortex are all features which are very closely simulated in the numerical solution. A similar high level of correlation is found to exist between the experimental and numerical flow patterns for other discrete times ranging over the entire phase 1 of flow during which the primary vortex develops from its birth to full maturity.

7. Conclusion

A general numerical method has been developed for the solution of the unsteady flow of a viscous incompressible fluid through axisymmetric duct geometries for which the variable axial contour may be described analytically in a piecewise-continuous manner by orthogonal co-ordinate systems. The discontinuities may include sharp corners. The method is applied specifically to simulate the flow through a spherical cavity approximating the geometry of the aortic root.

The numerical method uses finite-difference approximations of the vorticity and stream-function equations, and employs a hybrid-mesh design which permits a finer resolution of the flow near the solid walls where the gradients are high and, at the same time, maintains an overall economy of computer usage. The numerical scheme for the vorticity equation in each mesh subsystem uses central differences for the time and space derivatives except that second upwind differencing was used for the inertia terms. A Dufort–Frankel leapfrog approximation is also applied. The resulting scheme gives a stable solution with little loss of accuracy due to numerical damping. The elliptic stream-function equation is solved by optimized successive over-relaxation iterations. Guidelines are developed for the successful matching of flow variables at the interfaces between the hybrid mesh subsystems, and for the treatment of flow around a sharp corner.

The numerical results indicate, in detail, the birth and development of an annular vortex within the cavity as the flow accelerates from rest. The vortex grows to occupy most of the cavity. These results are in good agreement with observations made in an experimental flow-visualization study. The numerical simulation further yields detailed information about the emergence of secondary-flow features within the cavity, and about their role in a gradual degeneration of the primary vortex and in an apparent onset of physical instabilities. An accurate determination of the location of the reattachment stagnation point, a matter of significant importance in problems of enhanced heat transfer in the reattachment region, is made possible by the hybrid-mesh design. The solution also provides the spatial and temporal distribution of wall shear stress. Maximum shear levels attained and the time for which they persist are not judged sufficient to cause endothelial damage under the normal physiological conditions considered.

The work reported here was supported by the National Heart and Lung Institute of NIH under Grant no. HE-13803.

REFERENCES

Back, L. H. & Roschke, E. J. 1972 Shear-layer flow regimes and wake instabilities and reattachment lengths downstream of an abrupt circular channel expansion. *J. Appl. Mech. A.S.M.E.* 72–APM–2.

Batchelor, G. K. 1956 On steady laminar flow with closed streamlines at large Reynolds number. *J. Fluid Mech.* **1**, 177.

Bearman, P. W. 1965 Investigation of the flow behind a two-dimensional model with a blunt trailing edge and fitted with splitter plates. *J. Fluid Mech.* **21**, 241.

Bellhouse, F. J. 1969 Velocity and pressure distributions in the aortic valve. *J. Fluid Mech.* **37**, 587.

Bellhouse, B. J. & Talbot, L. 1969 The fluid mechanics of the aortic valve. *J. Fluid Mech.* **35**, 721.

Burggraf, O. R. 1966 Analytical and numerical studies of the structure of steady separated flows. *J. Fluid Mech.* **24**, 113.

Cheng, S. I. 1969 Accuracy of difference formulation of Navier–Stokes equations. *Phys. Fluids Suppl.* **12**, II 34.

Collins, W. M. & Dennis, S. C. R. 1973 Flow past an impulsively started circular cylinder. *J. Fluid Mech.* **60**, 105.

Courant, R., Isaacson, E. & Rees, M. 1952 On the solution of nonlinear hyperbolic differential equations by finite differences. *Comm. Pure Appl. Math.* **5**, 243.

Donovan, L. F. 1970 A numerical solution of unsteady flow in a two-dimensional square cavity. *A.I.A.A. J.* **8**, 524.

Dufort, F. C. & Frankel, S. P. 1953 Stability conditions in numerical treatment of parabolic differential equations. *Math. Tables & Other Aids to Comp.* **7**, 135.

Fromm, J. E. 1963 A method for computing unsteady, incompressible, viscous fluid flows. *Los Alamos Sci. Lab. Rep.* no. LA-2910.

Fromm, J. E. 1969 Numerical solutions of two-dimensional stall in fluid diffusers. *Phys. Fluids Suppl.* **12**, II 113.

Fry, D. L. 1968 Acute vascular endothelial changes associated with increased blood velocity gradients. *Circ. Res.* **22**, 165.

Gentry, R. A., Martin, R. E. & Daly, B. J. 1966 An Eulerian differencing method for unsteady compressible flow problems. *J. Comp. Phys.* **1**, 87.

Gillani, N. V. 1974 Time-dependent laminar incompressible flow through a spherical cavity. D.Sc. dissertation, Washington University.

Gosman, A. D., Pun, W. M., Runchal, A. K., Spalding, D. B. & Wolfshtein, M. 1969 *Heat and Mass Transfer in Recirculating Flows.* Academic.

Honji, H. 1975 The starting flow down a step. *J. Fluid Mech.* **69**, 229.

Honji, H. & Taneda, S. 1969 Unsteady flow past a circular cylinder. *J. Phys. Soc. Japan,* **27**, 1668.

Hung, T. K. & Schuessler, G. B. 1971 Computational analysis as an aid to the design of heart valves. *Chem. Engng Prog. Symp. Ser.* **67**, 8.

Keele, K. D. 1952 *Leonardo da Vinci on Movement of the Heart and Blood.* London.

Macagno, E. O. & Hung, T. K. 1967 Computational and experimental study of a captive annular eddy. *J. Fluid Mech.* **28**, 43.

Mehta, U. B. & Lavan, Z. 1969 Flow in a two-dimensional channel with a cavity. *N.A.S.A. Contractor Rep.* no. CR-1245.

Meisner, J. E. & Rushmer, R. F. 1963 Eddy formation and turbulence in flowing liquids. *Circ. Res.* **12**, 455.

Mueller, T. J. & O'Leary, R. A. 1970 Physical and numerical experiments in laminar incompressible separating and reattaching flows. *A.I.A.A. Paper,* no. 70-763.

O'Brien, G., Hyman, A. H. & Kaplan, A. S. 1951 A study of the numerical solution of partial differential equations. *J. Math. & Phys.* **29**, 223.

Pan, F. & Acrivos, A. 1967 Steady flows in rectangular cavities. *J. Fluid Mech.* **28**, 643.

Peskin, C. S. 1972 Flow patterns around heart valves: a numerical method. *J. Comp. Phys.* **10**, 252.

Rayleigh, Lord 1913 On the stability of the laminar motion of an inviscid fluid. *Scientific Papers*, vol. 6, p. 197. Cambridge University Press.

Richtmeyer, R. D. & Morton, K. W. 1967 *Difference Methods for Initial-Value Problems*, 2nd edn. Interscience.

Rimon, Y. 1969 Numerical solution of the incompressible time-dependent viscous flow past a thin oblate spheroid. *Phys. Fluids Suppl.* **12**, II 65.

Roache, P. J. 1972*a* *Computational Fluid Dynamics.* Hermosa.

Roache, P. J. 1972*b* On artificial viscosity. *J. Comp. Phys.* **10**, 169.

Roache, P. J. & Mueller, T. J. 1970 Numerical solutions of laminar separated flows. *A.I.A.A. J.* **8**, 530.

Scherer, P. W. 1973 Flow in axisymmetrical glass model aneurysms. *J. Biomech.* **6**, 695.

Schuessler, G. B. & Hung, T. K. 1972 Hemodynamics during the opening of a heart valve: a computational analysis. *25th Ann. Conf. Engng in Med. & Biol., Bel Harbour, Florida.*

Son, J. S. & Hanratty, T. J. 1969 Numerical solution for the flow around a cylinder at Reynolds numbers of 40, 200, 500. *J. Fluid Mech.* **35**, 369.

Swanson, W. M. & Clark, R. E. 1974 Dimensions and geometric relationships of the human aortic valve as a function of pressure. *Circ. Res.* **35**, 871.

Tani, I. 1968 Experimental investigation of flow separation over a step. In *Boundary Layer Research.* Springer.

Texon, M. 1957 The hemodynamic concept of atherosclerosis. *Arch. Int. Med.* **99**, 418.

Thoman, D. C. & Szewczyk, A. A. 1969 Time-dependent viscous flow over a circular cylinder. *Phys. Fluids Suppl.* **12**, II 76.

TOLLMIEN, W. 1936 General instability criterion of laminar velocity distributions. *N.A.C.A. Tech. Memo.* no. TM–792.

WESSLER, S. & YIN, E. T. 1969 On the mechanism of thrombosis. In *Progress in Hematology*, vol. 6, p. 201.

YOUNG, D. 1954 Iterative methods for solving partial differential equations of elliptic type. *Trans. Am. Math. Soc.* **76**, 92.

YOUNG, D. F. & SHIH, C. C. 1969 Some experiments on the effect of isolated protuberances on flow through tubes. *Experimental Mech.* (May).

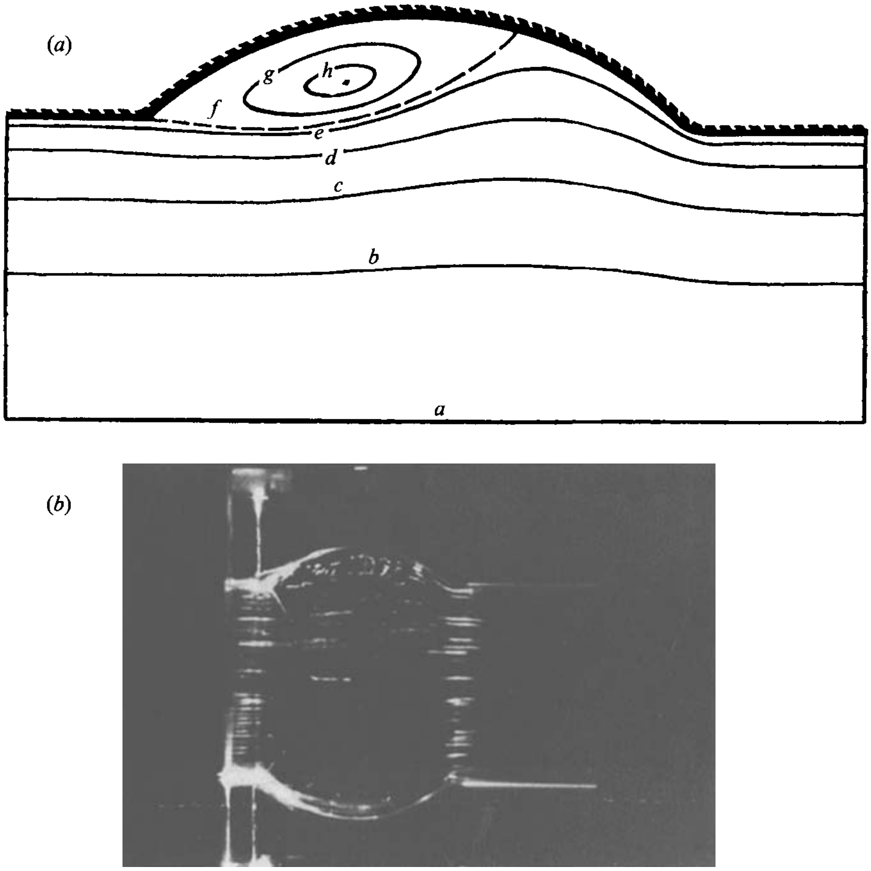

FIGURE 13. Comparison of numerical and experimental results. (*a*) Numerical plot of streamlines for $t' = 0{\cdot}120$. (*b*) Photograph exposure time corresponds to the period from $t' = 0{\cdot}120$ to $0{\cdot}133$.